ESKİŞEHİR TEKNİK ÜNİVERSİTESİ BİLİM VE TEKNOLOJİ DERGİSİ
B- TEORİK BİLİMLER

Eskişehir Technical University Journal of Science and Technology B- Theoretical Sciences

Estuscience – Theory, 2026, 14 (1) pp. 31-52 , DOI: 10.20290/estubtdb.1749220

RESEARCH ARTICLE

ELECTRONIC AND SPECTROSCOPIC PROPERTIES OF LUCIFERIN-DERIVED STRUCTURES: A DFT APPROACH

Sultan Funda EKTİ [1,*], Sevgi ŞEN [2]

[1] Department of Chemistry, Faculty of Science, Eskişehir Technical University, Eskişehir Tuürkiye.
sfekti@eskisehir.edu.tr - 0000-0001-6810-0030

[2] Department of Chemistry, Faculty of Science, Eskişehir Technical University, Eskişehir Tuürkiye.
sevgisen240@ogr.eskisehir.edu.tr - 0009-0001-7812-9336

Abstract

In this study, the structural, electronic, and spectroscopic properties of three luciferin derivatives (TPSS, PSS, and CSS) were comprehensively investigated using density functional theory (DFT) and time-dependent DFT (TD-DFT). In addition to geometry optimization and frequency analyses, HOMO–LUMO energy levels, UV–Vis absorption bands, IR vibrational spectra, and molecular electrostatic potential (MEP) maps were calculated. Dihedral angle analyses brought out the planarity and conformational stability of the molecules, while HOMO–LUMO energy gaps helped reveal their electronic excitation potentials. Electronic transitions and oscillator strengths computed via TD-DFT were employed to interpret the UV–Vis spectra based on the λmax values. IR data contributed to the identification of characteristic vibrational modes, and MEP maps offered a visual insight into electron density distributions and potential reactive regions. All results were comparatively evaluated for the gas phase as well as in DMSO and $CHCl_3$ solvent environments, providing a theoretical basis for understanding the behavior of these luciferin derivatives.

Keywords

Luciferin,
Density Functional Theory,
HOMO-LUMO energy gap,
Molecular modelling

Time Scale of Article

Received :23 July 2025
Accepted : 27 October 2025
Online date : 25 February 2026

1 INTRODUCTION

Throughout human history, nature has been a notable source of inspiration for scientific exploration and technological progress. The biological traits acquired by living organisms during evolution have not only ensured their survival but have also contributed to the emergence of new research fields in science and technology. One impressive example is bioluminescence, the natural ability of some organisms to produce visible light through chemical reactions. This fascinating phenomenon has caught the attention of researchers across many fields, from molecular biology and biotechnology to quantum chemistry. Understanding this natural light-emission mechanism and modelling its structural components is of great importance in both fundamental sciences and applied fields such as optoelectronics and sensor technologies [1-5].

One of the most well-documented examples of bioluminescence in nature is the firefly. These organisms produce light through a chemical reaction that occurs within their bodies. In this reaction, the substrate luciferin is oxidised by molecular oxygen in the presence of the luciferase enzyme. Firefly luciferin is a heterocyclic compound formed by the combination of a benzothiazole ring and thiazole-4-carboxylic acid. This compound interacts with the active site of the luciferase enzyme, enabling the bioluminescent reaction to occur. When luciferin undergoes oxidation, it is converted into oxyluciferin, the oxidized form of the molecule (Figure 1). Oxyluciferin has a more extended conjugation system compared to luciferin, which results in greater electron delocalization. In firefly bioluminescence, D-luciferin is first

*Corresponding Author: sfekti@eskisehir.edu.tr

activated with the help of ATP and magnesium ions. It then reacts with oxygen to form an excited oxyluciferin molecule. As this molecule returns to its ground energy state, it emits a photon (light) along with byproducts such as carbon dioxide, AMP, and pyrophosphate (Figure 2). The colour of the emitted light can vary from yellow to red, depending on the type of luciferase involved [6-9].

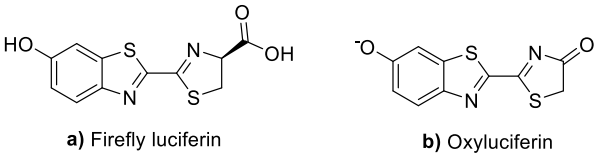

Figure 1. Chemical structures of firefly luciferin and oxyluciferin

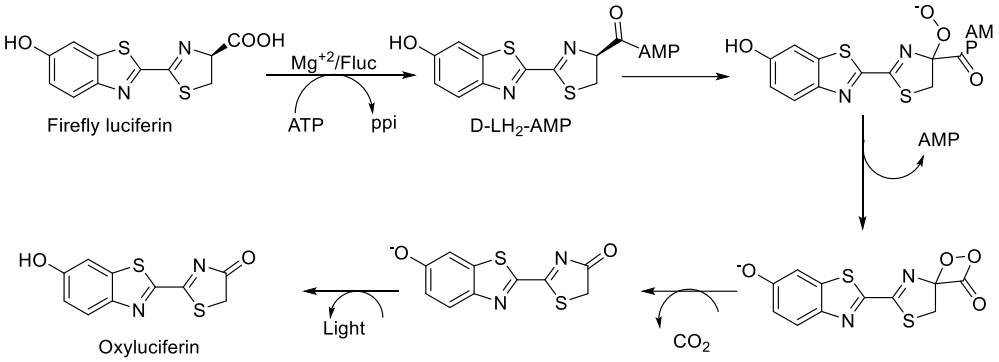

Figure 2. Mechanism of firefly bioluminescence

The bioluminescence mechanism is no longer limited to biological organisms but is now finding diverse applications in scientific and technological fields. In particular, the luciferin–luciferase system has versatile uses in pharmaceutical and biotechnology. It is applied in oncological research for monitoring tumor growth, visualizing vaccine efficacy, and tracking the biodistribution of drugs. In neuroscience, optogenetic methods employ light-sensitive proteins to study brain activities.

Beyond that, the nature-inspired aspect of bioluminescence contributes to the development of sustainable technologies. For example, the "Glowing Plant" project aims to genetically modify plants to emit light in the dark. Such biomimetic approaches hold promise for developing natural light sources that could replace artificial lighting systems in the future. These innovations contribute to energy savings and environmental sustainability goals, further expanding the potential application areas of bioluminescence [10].

Considering these insights, the computational design of luciferin derivatives holds critical importance for both a deeper understanding of bioluminescence mechanisms and the design of next-generation bioluminescent systems [11,12]. Structural changes, particularly the extension of π-conjugation systems [1,13,14], diversification of electron donor-acceptor interactions [15] and reconfiguration of heteroaromatic rings [16,17], can significantly influence the photophysical and optoelectronic properties of these systems.

Structural modifications of the luciferin molecule directly influence optimizing the desired photophysical properties in bioluminescent systems. A commonly reported approach in the literature involves substituting various functional groups at specific positions on the luciferin scaffold, such as the 2nd, 5th, and 6th positions. Additionally, different positional linkages are established through the luciferin core structure (Figure 3). These positional modifications directly influence the electronic

distribution of the molecule, thereby playing a crucial role in determining light intensity, color, and quantum yield [1,13-18].

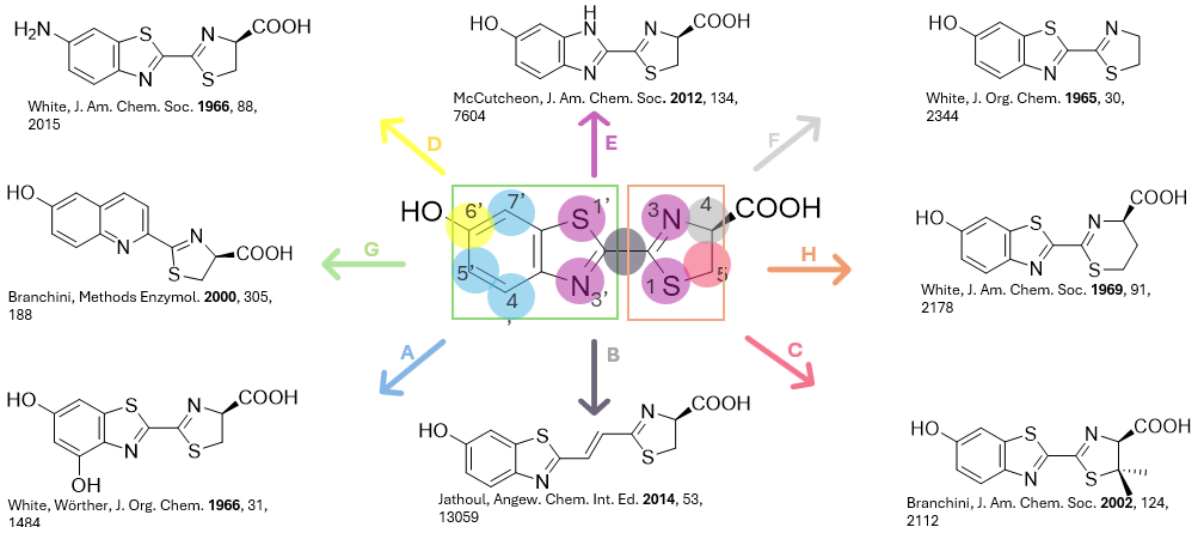

Figure 3. Bindings from different positions of luciferin

The extension of the π-conjugation system facilitates a red shift in light emission, enabling the release of low-energy photons. To enhance π-conjugation between donor (D) and acceptor (A) groups, conjugated linkers such as phenyl, phenol, or vinyl are introduced (Figure 4). These D–π–A structures improve both the light absorption and emission capabilities of the molecule. Additionally, they facilitate charge transfer, thereby increasing the stability of the excited state and reducing the HOMO–LUMO energy gap; consequently, the transition from the excited state to the ground state becomes more efficient [19] .

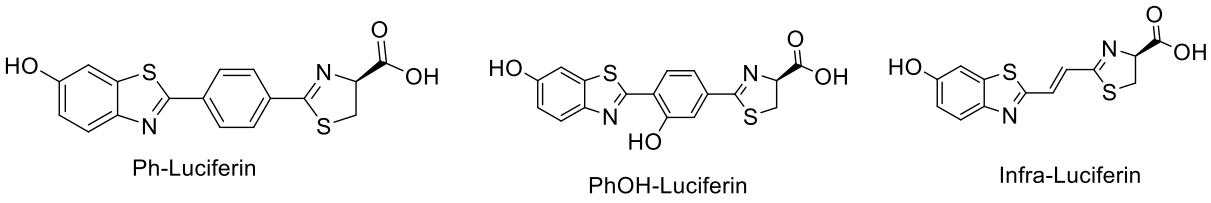

Figure 4. Modifications to enhance conjugation of luciferin derivatives

Furthermore, the introduction of amino groups (e.g., $–NH_2$, $–N(CH_3)_2$) into the luciferin structure not only increases the electron density of the molecule but also supports charge transfer by establishing donor–acceptor systems. Consequently, the excited-state stability is enhanced, significantly improving bioluminescence efficiency. For instance, 4'-amino-substituted D-luciferin derivatives are notable in the literature for providing both brighter and longer-lasting light emission (Figure 5) [16-19] .

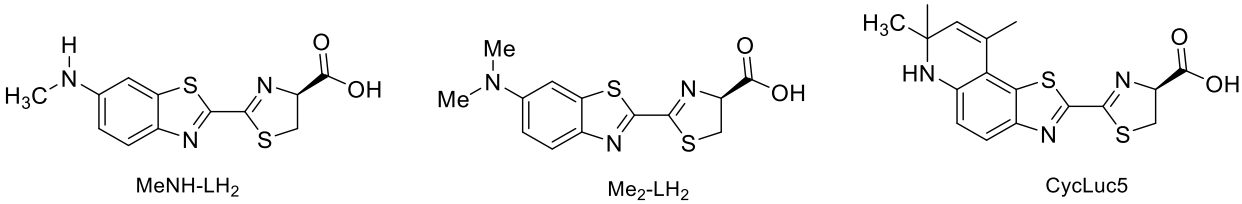

Figure 5. Luciferin derivatives obtained by attaching amino groups

Computational studies have demonstrated that structural modifications on the luciferin molecule directly influence the HOMO–LUMO energy gap, which in turn determines the wavelength of light emission and quantum yield [13,18]. Particularly, donor–π–acceptor systems formed by appropriately positioning electron-rich (donor) and electron-deficient (acceptor) groups within the same molecule facilitate efficient electron transfer in the excited state [14]. This strategy not only advances the development of bioluminescent systems but also provides a valuable approach for designing novel molecules in various optoelectronic applications, such as OLEDs, sensor technologies, and bioimaging [20].

The originality of this study stems from the incorporation of a thiophene ring, which serves as an aromatic heterocyclic bridge between two aromatic structures common to all three molecules. In the literature, several studies have reported the incorporation of benzene or vinyl groups into similar luciferin derivatives [19]; however, the introduction of a thiophene ring between these aromatic structures is proposed for the first time in this work. This structural modification extends the π-conjugation system, resulting in significant alterations in the electronic and spectroscopic properties of the molecules.

These effects were thoroughly investigated using Density Functional Theory (DFT) and Time-Dependent DFT (TD-DFT) calculations. In addition, the influence of various substituent rings on the HOMO–LUMO energy gap and UV–Vis spectral behavior was systematically analyzed. Specifically, the thiazolo[4,5-b]pyridine ring in TPSS, the aliphatic cyclohexyl substituent in CSS, and the 4-methoxybenzene ring in PSS each exert distinct effects on the degree of conjugation and overall electronic distribution. The impact of replacing the benzothiazole ring with a thiazolo[4,5-b]pyridine ring on electron delocalization within the aromatic structure was also examined (TPSS). Furthermore, the thiophene ring, a structure commonly utilized in light-based technologies [21], was integrated into the molecular scaffold to further enhance π-conjugation and strengthen donor–acceptor interactions. The effects of this modification on HOMO–LUMO energy gap is evaluated in detail. For comparative purposes, two additional derivatives were studied: an aliphatic cyclohexyl-substituted analog lacking aromaticity (CSS) and a 4-methoxybenzene-based reference compound with a strong electron-donating effect (PSS).

Among these, the PSS molecule is expected to display the most distinctive electronic behavior. The methoxy group introduces a strong donor–π–acceptor (D–π–A) interaction within the molecular structure, redistributing electron density and leading to the narrowest HOMO–LUMO energy gap among the studied systems. This feature suggests that electronic transitions in the excited state may potentially result in longer-wavelength emissions. Consequently, the PSS structure can be regarded as a promising candidate not only for understanding the electronic properties of luciferin-based systems but also for advancing bioluminescence and optoelectronic applications (Figure 6).

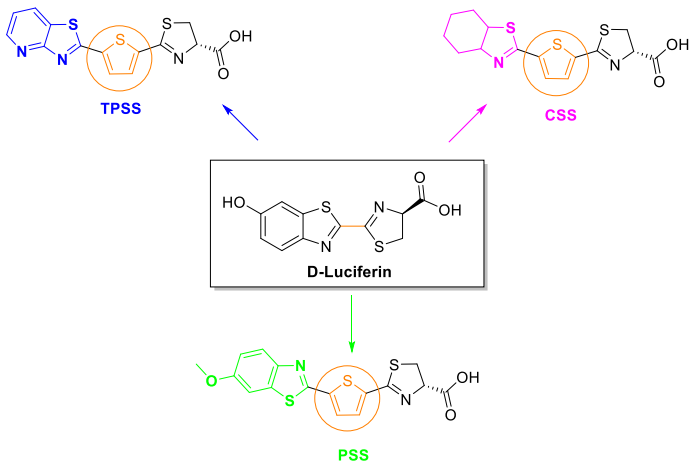

Figure 6. The luciferin structure and its three molecular modifications (TPSS, CSS, PSS). The colored fragments highlight the substituted groups, while the circled thiophene ring emphasizes its key role in enhancing π-conjugation.

Within the scope of this study, DFT calculations for the target molecules were performed using the B3LYP method in 6-31G(d, p) double zeta basis set. This combination is known to provide reliable results for organic systems with conjugation [22].

As a result of the calculations, conformational analyses of the molecules were conducted, and their IR and NMR spectra, along with excited-state energies, were computed. Furthermore, the HOMO–LUMO frontier orbitals and their energy gaps were determined, providing insights into the electronic transition properties of the molecules. Based on the obtained theoretical data, the spectral and electronic properties expected upon synthesis of these molecules were predicted.

In conclusion, this study demonstrates that next-generation luciferin derivatives inspired by nature can be developed through computational chemistry techniques. This approach is expected to contribute to a deeper understanding of bioluminescence mechanisms at the molecular level.

2. METHODS

In this study, theoretical modelling of three different molecules, namely TPSS, CSS, and PSS, was performed. Density Functional Theory (DFT) and Time-Dependent DFT (TD-DFT) methods were employed to investigate the structural, electronic, and spectral properties of the molecules. These approaches are known to provide high accuracy in predicting the electronic structures, conformational characteristics, and light-emission behaviours of medium-sized organic systems. The reliability of these methods for such predictions is well-documented in the literature for a range of similar systems [23-25].

All quantum chemical calculations were carried out using the Gaussian 09W software [26]. B3LYP hybrid functional was chosen due to its widespread use in structural optimization, spectral prediction (IR, NMR), and optoelectronic characterization of organic molecules. Geometry optimizations and frequency calculations were carried out using the B3LYP functional in 6-31G(d,p) basis [22]. For solvent-phase calculations (DMSO and $CHCl_3$), the Conductor-like Polarizable Continuum Model (CPCM) was employed to simulate the solvent environment [27]. Owing to the incorporation of polarization functions, this basis set allows for a more accurate description of conjugated systems, variations in bond angles, dipole moments, and charge transfer processes. Furthermore, the 6-31G(d,p) basis set is recognized for its reliability in precisely representing electron density distributions and bonding characteristics in π-conjugated and aromatic systems [14]. In the initial stage, the possible conformations of each molecule were pre-optimized using the MM2 and MMFF94 force fields. These force fields enable a rapid and efficient exploration of conformational space, facilitating the identification of low-energy structures. Among the obtained conformers, the most stable ones were selected as starting points for advanced quantum chemical calculations. Subsequent geometry optimizations were performed, and frequency analyses were carried out to verify that the optimized structures correspond to true minima on the potential energy surface.

Excited-state energy levels were evaluated using the TD-DFT method to gain insight into the electronic transition characteristics of the molecules. This analysis is crucial for predicting optical transitions, absorption properties, and potential emission behaviours. Furthermore, theoretical NMR chemical shifts and IR vibrational modes were calculated to provide reference spectral data that can support the experimental characterization of the target molecules.

The computational investigations were not restricted to the gas phase; additional calculations were conducted in solvent environments, such as DMSO and $CHCl_3$, to assess the influence of solvent effects on the electronic structure and spectral properties.

Through this comprehensive computational strategy, detailed information on the minimum energy conformations, HOMO–LUMO frontier orbitals, energy gaps, molecular electrostatic potential (MEP) distributions, and emission potentials of the molecules was obtained. Theoretical predictions of IR and NMR spectra were also generated, offering reliable data to guide experimental studies. Overall, the theoretical findings contribute to a deeper understanding of the bioluminescence mechanism at the molecular level and provide a solid theoretical framework for the rational design of novel luciferin derivatives.

3. RESULTS and DISCUSSIONS

In this section, the structural, electronic, and spectral data obtained from the theoretical calculations are comprehensively presented and critically discussed. For the investigated molecules, geometry optimizations, HOMO–LUMO energy gaps, UV-Vis transition characteristics, IR and NMR spectral predictions, and electrostatic potential distributions have been thoroughly analyzed. Based on these findings, particular emphasis has been placed on evaluating the emission potential of the TPSS compound and its suitability for bioluminescence applications. Within each subsection, the results are interpreted from both quantitative and qualitative perspectives, providing a comparative assessment of the effects of molecular modifications.

3.1. Geometry Optimization

Optimized geometries provide valuable insight into the structural parameters that govern conjugation and molecular stability. The most stable conformations of the target molecules were optimized at the B3LYP/6-31G(d,p) level of theory (Figure 7). Following the optimization, the dihedral angles were examined to evaluate structural features such as planarity, π-conjugation, and ring deformation.

The dihedral angles around the single bonds throughout the molecule, obtained from the DFT calculations, are listed in Table 1. The dihedral angles between the N7–C8–C10–S14 and S14–C13–C15–S19 atoms were found to be approximately 0˚ or very close to 180˚ in both the gas phase and solvent environments. This indicates that the molecules exhibit a largely planar structure, there by maintaining effective π-conjugation. These results are consistent with previous studies on native D-luciferin, which also revealed that the molecule has a largely planar configuration [14].

In contrast, the dihedral angles between the N16–C17–C20–O22 atoms were calculated to be in the range of 67–96˚ for all compounds. This deviation suggests that these groups are twisted relative to the core structure. Such a distortion implies that the carboxylic acid group is almost perpendicular to the thiazole ring, resulting in a disruption of π-conjugation at this point. In addition to dihedral angles, selected bond lengths were also examined to further characterize the optimized structures. The C–S bond length was found to be approximately 1.74 Å and the C–N bond length was approximately 1.30 Å, with no significant difference observed between the gas and solvent phases (Table 2).

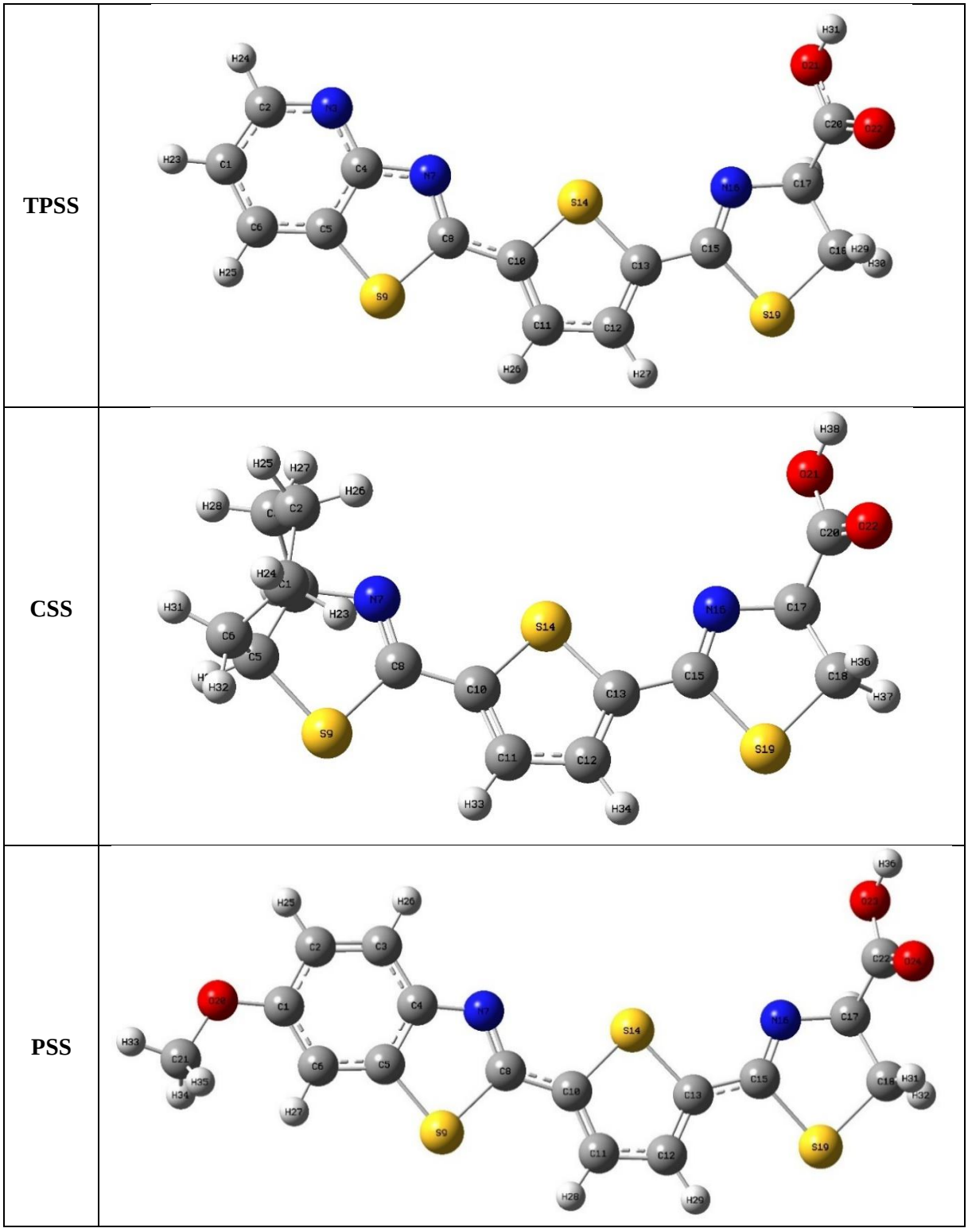

Figure 7. Three-dimensional representations of TPSS-CSS-PSS structures

Table 1. Dihedral angle (in degree) of TPSS-CSS-PSS molecules

Molecule	Atom Numbers	Gas	DMSO	$CHCl_3$
TPSS	N_7-C_8-C_{10}-S_{14}	0.1	0.3	0.2
	S_{14}-C_{13}-C_{15}-S_{19}	174.2	172.9	174.2
	N_{16}-C_{17}-C_{20}-O_{22}	75.5	68.8	70.6
CSS	N7-C_8-C_{10}-S_{14}	4.4	4.5	4.5
	S_{14}-C_{13}-C_{15}-S_{19}	173.7	174.5	174.3
	N_{16}-C_{17}-C_{20}-O_{22}	75.6	67.9	69.7
PSS	N_7-C_8-C_{10}-S_{14}	0.02	0.02	0.02
	S_{14}-C_{13}-C_{15}-$S1_9$	175.2	175.2	175.2
	C_{16}-N_{17}-C_{22}-O_{24}	95.7	95.7	95.7

Table 2. Bond lengths (Å) of TPSS-CSS-PSS molecules

	TPSS			**CSS**			**PSS**		
Bond Length	**Gas**	**DMSO**	**$CHCl_3$**	**Gas**	**DMSO**	**$CHCl_3$**	**Gas**	**DMSO**	**$CHCl_3$**
C_8-C_9	1.806	1.794	1.788	1.802	1.802	1.802	1.874	1.874	1.874
N_7-C_8	1.310	1.298	1.302	1.276	1.276	1.276	1.302	1.302	1.302
C_8-C_{10}	1.430	1.446	1.446	1.457	1.457	1.457	1.433	1.433	1.433
C_{10}-S_{14}	1.731	1.745	1.747	1.744	1.744	1.744	1.812	1.812	1.812
C_{13}-S_{14}	1.729	1.744	1.746	1.745	1.745	1.745	1.813	1.813	1.813
C_{13}-C_{15}	1.436	1.454	1.455	1.454	1.454	1.454	1.440	1.440	1.440
N_{16}-C_{15}	1.290	1.230	1.281	1.280	1.280	1.279	1.286	1.286	1.286
C_{15}-S_{19}	1.800	1.802	1.800	1.803	1.803	1.803	1.875	1.875	1.875
N_{16}-C_{17}	1.478	1.463	1.465	1.463	1.462	1.462	1.481	1.481	1.481
C_{17}-C_{20}	1.532	1.533	1.533	1.532	1.532	1.532	1.523	1.523	1.523
C_{20}-O_{22}	1.207	1.210	1.212	1.210	1.210	1.210	-	-	-
C_{20}-O_{21}	1.366	1.346	1.342	1.346	1.346	1.346	-	-	-
C_{22}-O_{24}	-	-	-	-	-	-	1.232	1.232	1.232
C_{22}-O_{23}	-	-	-	-	-	-	1.370	1.370	1.370

3.2. IR Spectrum Analysis

The theoretical infrared (IR) spectra of the optimized molecular structures were obtained using the Gabedit software. Based on DFT frequency calculations, characteristic vibrational modes specific to each compound were identified, and the bands corresponding to structural functional groups were analyzed in detail. In this context, vibrational frequencies corresponding to key functional groups such as C=O, C=N, C=C and C–S were comparatively reported.

When the IR spectra of all compounds (Figure 8-10) calculated in the gas phase and solvent environments (DMSO and $CHCl_3$ under the CPCM model) were examined. It was observed that some characteristic vibrational modes exhibited noticeable shifts in wavenumber due to solvent effects. In particular, the O–H stretching vibration of the carboxylic acid group shifted to lower frequencies compared to the gas phase, appearing as a broad band around 3400 cm^{-1} in solvent environments. This red shift indicates the presence of hydrogen-bonding interactions and solvent–solute effects. The C=O stretching vibrations were observed in the range of 1700–1725 cm^{-1}, showing slight decreases in frequency in polar solvents. Aromatic C–H stretching vibrations remained stable within the 3060–3075 cm^{-1} range, while aliphatic C–H vibrations were detected only in the CSS molecule between 3250–2900 cm^{-1}. In the PSS molecule, the C–O stretching band corresponding to the methoxy group was observed around 1250–1020 cm^{-1}. The C–S stretching vibrations, attributed to thiophene, thiazole, and thioester

groups, appeared in the range of 700–500 cm^{-1} for all compounds, exhibiting slight blue shifts under solvent influence. These findings indicate that solvent polarity has a pronounced effect particularly on groups capable of hydrogen bonding, such as O–H and C=O. These data provided important structural information to confirm the presence of functional groups.

Table 3. Characteristic IR data for the studied compounds

Bond	Functional Group	Wavenumber Range (cm^{-1})	Molecule(s)
O–H stretching	Carboxylic acid group	3600	All compounds
C–H stretching (aromatic)	Aromatic rings	3060–3075	All compounds
C–H stretching (aliphatic)	Alkyl groups	3250–2900	Only CSS
C–H bending (aromatic)	Aromatic rings	1850–1750	All compounds
C=O stretching	Carbonyl group	1700–1725	All compounds
C=N stretching	Imine group	1610–1630	All compounds
C=C stretching	Aromatic system	1550–1200	All compounds
C–O stretching	Methoxy group	1250–1020	Only PSS
C–S stretching	Thiophene-thioeter-thiazole	700–500	All compounds

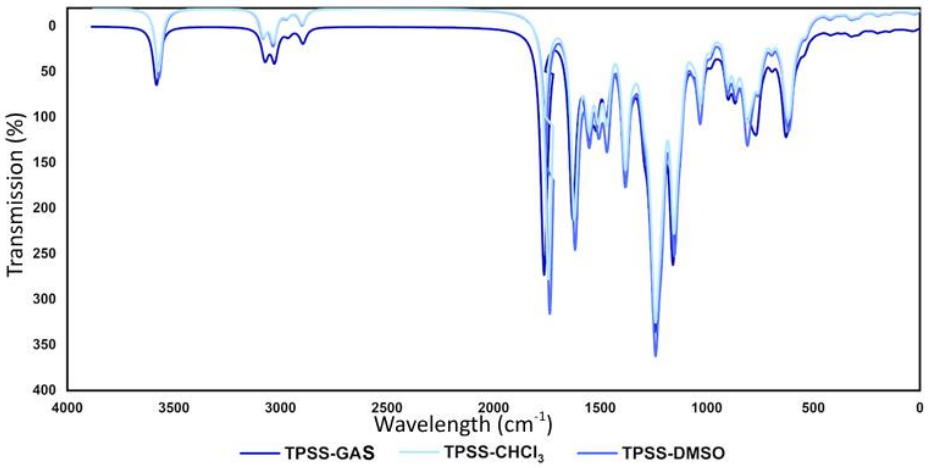

Figure 8. The Calculated IR Spectrum of the TPSS Molecule in the Studied Solvents

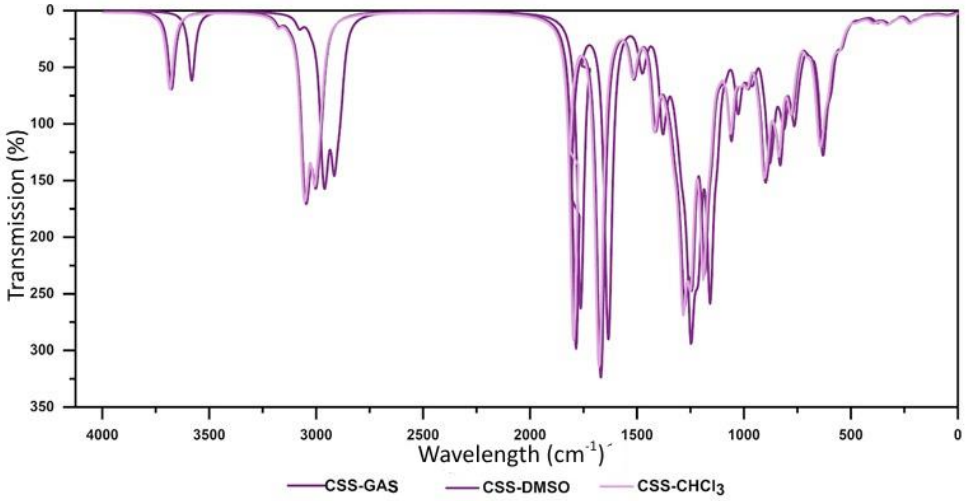

Figure 9. The Calculated IR Spectrum of the CSS Molecule in the Studied Solvents

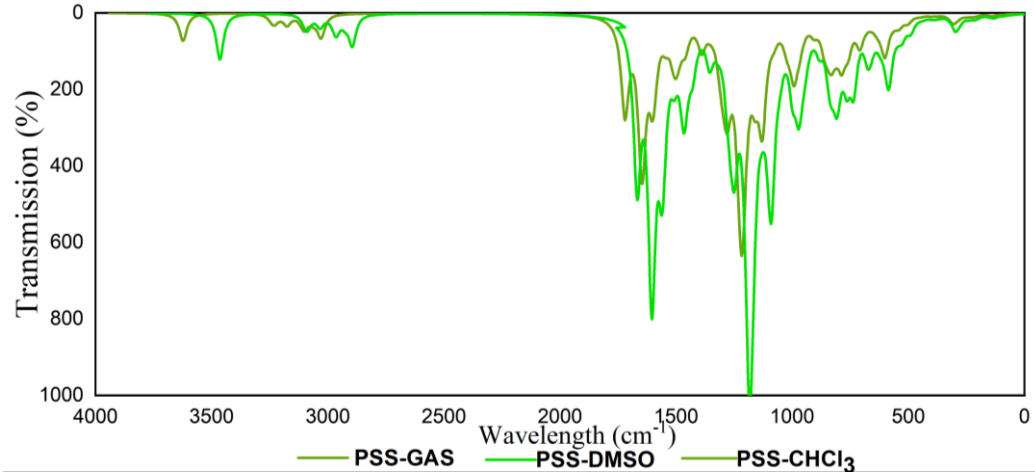

Figure 10. The Calculated IR Spectrum of the PSS Molecule in the Studied Solvents

Note: *For the present level of theory (B3LYP/6-31G(d,p)), all the spectra were scaled by a factor of 0.9627 for the wavenumbers [28]*

3.3. Analysis of UV-Vis Spectrum

The excited-state energy levels of the molecules were calculated using the TD-DFT method, and the corresponding theoretical UV-Vis absorption spectra were obtained (Figure 11-13).Theoretical UV-Vis spectra obtained from the calculations indicate that the fundamental electronic transitions of the studied molecules are largely π–π* in character, with a smaller contribution from n–π* transitions.

The TPSS compound exhibits typical π–π* transitions, with absorption bands starting around 310 nm in the gas phase and shifting to 375 nm due to the solvent effect. A characteristic red shift is effective with increasing solvent polarity. In the CSS compound, due to the cyclohexane ring's lack of aromaticity and limited conjugation, π–π* transitions occur at shorter wavelengths (275–350 nm), indicating a wider HOMO–LUMO energy range, consistent with the blue shift. In the PSS compound, the π-electron density increases due to the electron-donating effect of the methoxy group, which increases the degree of conjugation of the molecule and narrows the HOMO–LUMO energy range. Therefore, PSS exhibits absorption bands in the 340–430 nm range, extending not only into the ultraviolet region but also into the visible region. Furthermore, the presence of n–π* contributions in some low-energy bands in PSS causes further broadening of the absorption. Generally, increasing solvent polarity led to a regular redshift in the π–π* transitions in all compounds. This observation suggests that environments with dielectric constants of 1 (gas phase), 4.81 ($CHCl_3$), and 46.7 (DMSO) stabilize the excited states to different extents. As the dielectric constant increases, stronger solute–solvent interactions result in a gradual reduction of the HOMO–LUMO energy gap compared to the gas phase.

In conclusion, the PSS compound stands out as the molecule with the lowest energy difference due to its absorption extending into the visible region. Therefore, the PSS molecule is predicted to be the compound with the highest potential red shift among the three structures examined. These findings clearly demonstrate the critical role played by both the aromatic rings in the molecular structure and the solvent environments on the electronic transitions.

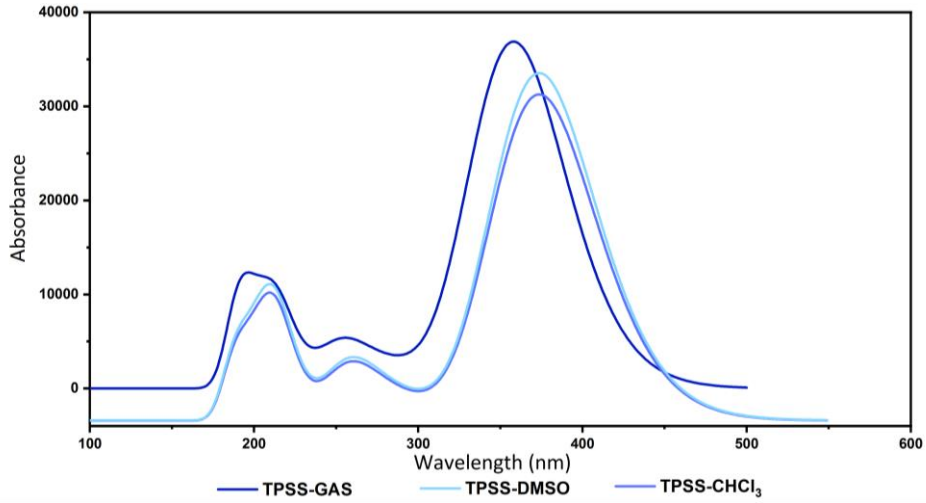

Figure 11. Theoretical UV-Vis Spectra of the TPSS Molecule

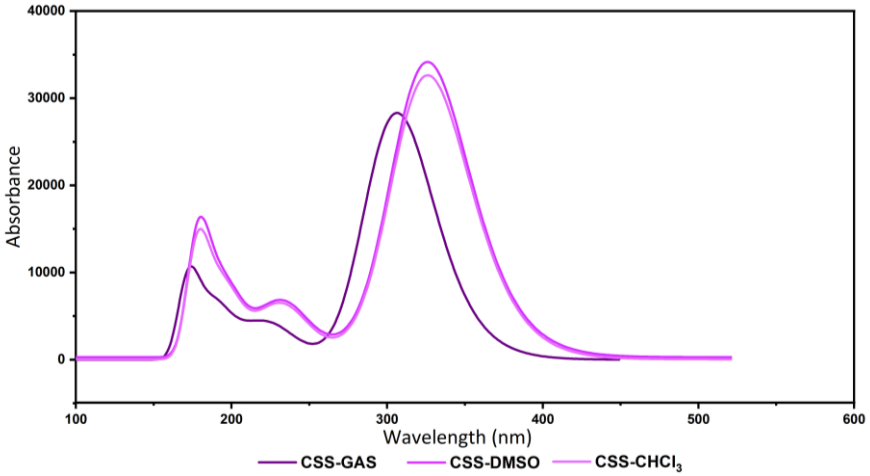

Figure 12. Theoretical UV-Vis Spectra of the CSS Molecule

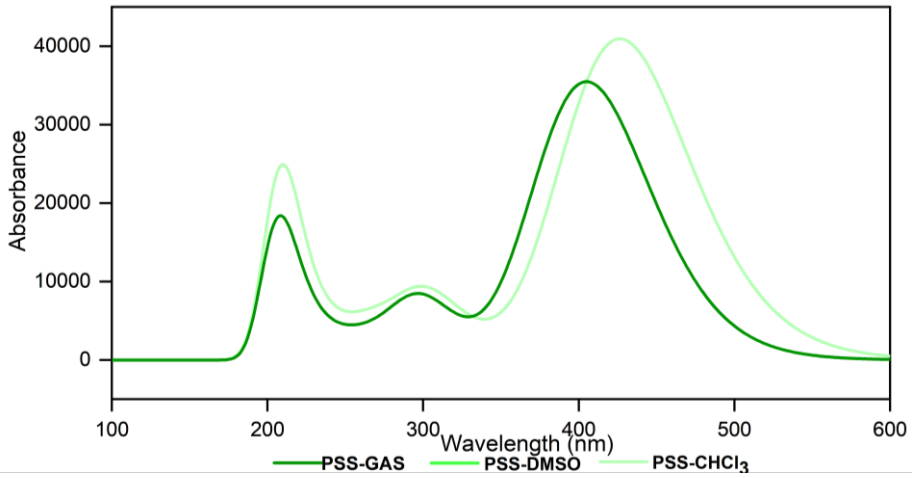

Figure 13. Theoretical UV-Vis Spectra of the PSS Molecule

The electronic properties of the molecules were evaluated based on the energies of the Highest Occupied Molecular Orbital (HOMO) and the Lowest Unoccupied Molecular Orbital (LUMO). The HOMO–LUMO energy gap (ΔE) is a critical parameter that reflects the chemical reactivity, photophysical behaviour, and light emission potential of the molecules. In this context, DFT and TD-DFT calculations

were performed in both the gas phase and solvent environments (DMSO and $CHCl_3$) for the TPSS, CSS, and PSS compounds, considering 50 excited states to determine the excitation energy levels.

According to the results obtained, the PSS compound exhibited a lower HOMO–LUMO energy gap compared to the two reference molecules. This indicates that the excitation transitions of TPSS occur at lower energies, making it more advantageous in terms of optoelectronic properties such as light emission. The calculated energy gaps for TPSS were found to be 3.52 eV in the gas phase, 3.34 eV in DMSO, and 3.35 eV in $CHCl_3$ (Figure 14). For the PSS compound containing a methoxy group, the corresponding values were 3.09 eV, 2.91 eV, and 2.92 eV (Figure 15). In contrast, the CSS compound with a cyclohexane ring exhibited significantly larger energy gaps of 4.76 eV in the gas phase, 4.16 eV in DMSO, and 4.23 eV in $CHCl_3$ (Figure 16).

These energy differences are directly related to the level of aromaticity and the effectiveness of π-conjugation within the molecular structures. In the TPSS compound containing a pyridine ring, the conjugation system is sustained continuously across the molecule, resulting in a narrower energy gap. In contrast, the CSS compound, which features a non-aromatic cyclohexane ring, exhibits reduced conjugation efficiency, leading to an increased energy gap.

Furthermore, analysis of orbital transition contributions revealed that the HOMO→LUMO transitions dominate, with a contribution of 93–99% in the TPSS compounds, contribution of 88-99% in the PSS compounds, whereas in the CSS compound, this contribution ranges between 74% and 85% (Table 4).

When these results are considered alongside the HOMO–LUMO energy gaps, it becomes evident that the TPSS and PSS molecules possesses more intense and characteristic orbital contributions in its electronic transitions. Consequently, the excited-state properties of TPSS and PSS are sharper and more predictable, which supports its advantage in potential light-emitting and optoelectronic applications.

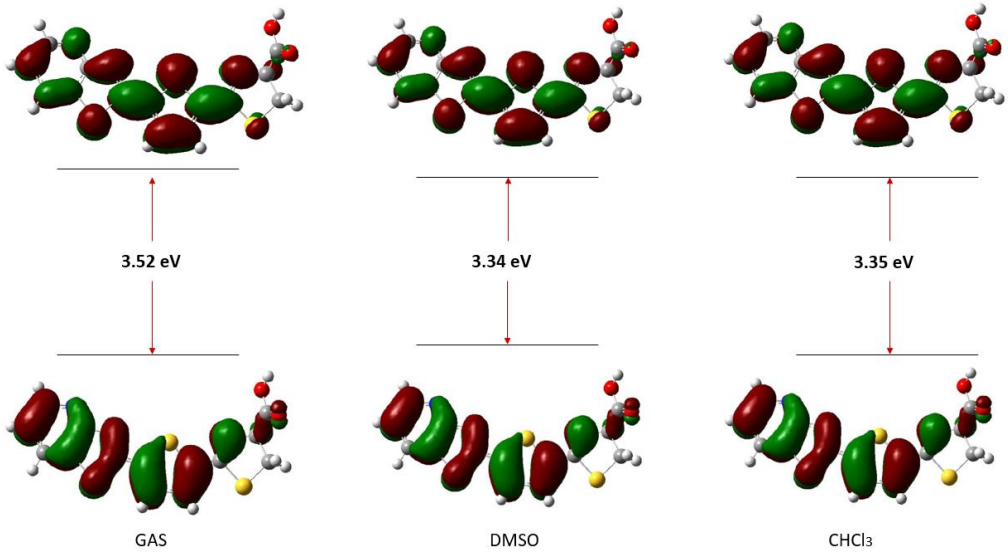

Figure 14. Calculated HOMO–LUMO frontier orbitals and band energy gaps of the TPSS molecule

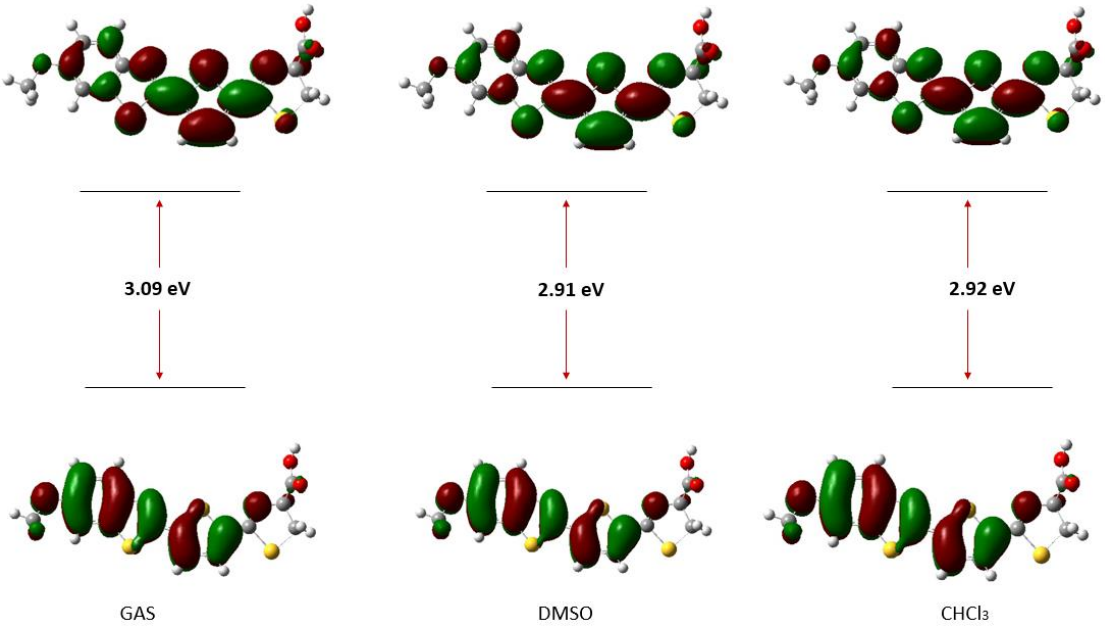

Figure 15. Calculated HOMO–LUMO frontier orbitals and band energy gaps of the PSS molecule

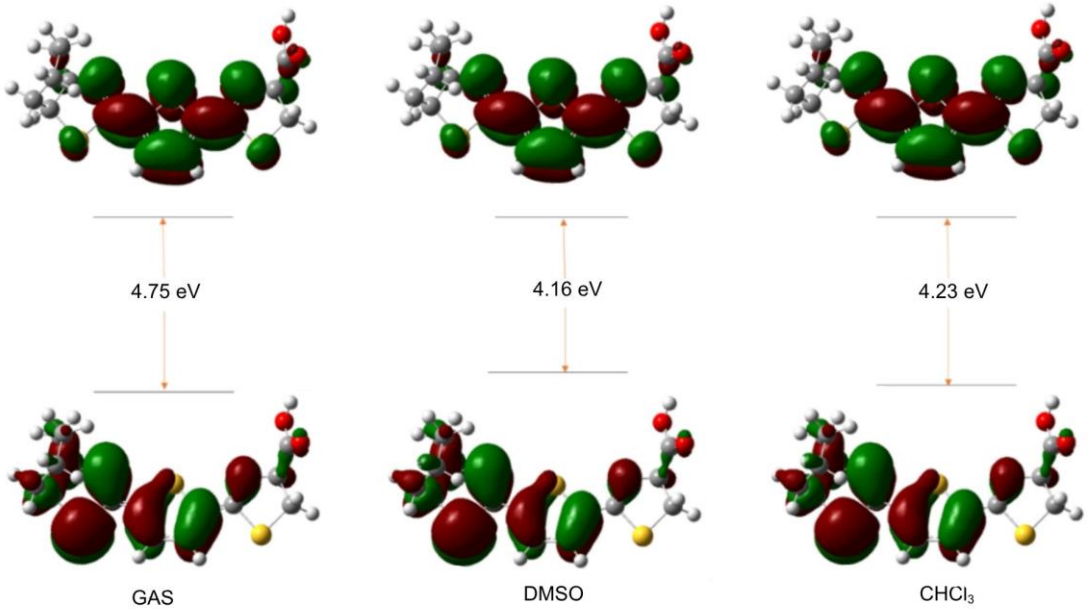

Figure 16. Calculated HOMO–LUMO frontier orbitals and band energy gaps of the CSS molecule

Table 4. λ_{max} values and Contribution of the Compounds

Compounds	Phase	State	Wavelength (λ_{max})	Oscillator Strength (*f*)	Contribution
TPSS	GAS	S1	359.42	0.8398	H->L (98%)
		S2	343.99	0.0793	H-1->L (98%)
		S3	315.86	0.0001	H-3->L (94%)
	DMSO	S1	374.61	1.0172	H->L (99%)
		S2	349.16	0.0468	H-1->L (99%)
		S3	304.37	0.0002	H-3->L (93%)
	$CHCl_3$	S1	374.19	1.0272	H->L (99%)
		S2	347.97	0.0458	H-1->L (99%)
		S3	307.04	0.0001	H-3->L (93%)
PSS	GAS	S1	405.32	0.8717	H->L (99%)
		S2	351.09	0.0101	H-1->L (93%)
		S3	340.97	0.0152	H-2->L (93%)
	DMSO	S1	428.34	0.993	H->L (99%)
		S2	353.55	0.0272	H-1->L (88%)
		S3	349.66	0.0144	H-2->L (89%)
	$CHCl_3$	S1	426.66	1.0078	H->L (99%)
		S2	352.72	0.0218	H-1->L (88%)
		S3	347.74	0.0172	H-2->L (89%)
CSS	GAS	S1	342.13	0.0326	H->L (76%)
		S2	295.54	0.0117	H-4->L (79%)
		S3	276.93	0.001	H-5->L (85%)
	DMSO	S1	348.97	0.0522	H->L (85%)
		S2	329.01	0.0854	H-1->L (75%)
		S3	312.83	0.6938	H-2->L (79%)
	$CHCl_3$	S1	347.39	0.0564	H->L (84%)
		S2	327.98	0.0988	H-1->L (74%)
		S3	312.67	0.6834	H-2->L (80%)

It is important to mention that the energy gaps obtained from UV–Vis spectra through TD-DFT calculations reflect optical band gaps, whereas the values estimated from the HOMO–LUMO energy difference correspond to electrical band gaps. In general, optical gaps appear smaller because the excited electron remains partially bound to the hole by Coulombic attraction, which slightly lowers the overall excitation energy compared with the electrical gap [29].

3.4. NMR Spectral Analysis

The theoretical ^{1}H-NMR and ^{13}C-NMR spectra of TPSS, CSS, and PSS compounds were calculated using the FACIO software [30] at the 6-31G(d,p) level of theory in both DMSO and $CHCl_3$ solvent environments to investigate their structural and electronic properties. The obtained chemical shift values (δ, ppm) provide detailed insights into the electronic environments of the atoms, confirming the presence of aromatic, heterocyclic, and aliphatic groups, as well as functional groups such as carboxylic acids and methoxy moieties. The calculated shifts reflect the effects of π-conjugation, hydrogen-bonding interactions, and magnetic anisotropy arising from neighboring heteroatoms, thereby facilitating the understanding of the structural features of the molecules. Only minor solvent-dependent variations (within ±0.5 ppm) were observed, indicating that the calculated data are reliable and that solvent effects are minimal (Tables 5–7). Furthermore, comparison among TPSS, CSS, and PSS demonstrates how the attachment of different functional groups modifies the electronic environment and influences both proton and carbon chemical shifts, clearly showing that the calculated values are in good agreement with theoretical expectations. The NMR calculations were performed using TMS as the reference.

3.4.1. TPSS compound

Table 5. Calculated NMR Results of the TPSS Compound

		DMSO	$CHCl_3$
	Atom	**Chemical Shift**	**Chemical Shift**
^{13}C-NMR	**1**	125.6432	125.1016
	2	154.5018	154.4287
	4	168.5098	168.7912
	5	142.5545	142.2839
	6	136.6460	135.6975
	8	174.6531	173.9785
	10	154.3696	154.7440
	11	133.7449	132.7974
	12	137.5455	136.8194
	13	153.3663	153.7250
	15	172.1711	171.7047
	17	88.9301	88.9476
	18	49.1768	49.2188
	20	177.1199	176.7288
^{1}H-NMR	**23**	7.9072	7.8161
	24	9.1704	9.1756
	25	8.8609	8.7594
	26	8.2087	8.1174
	27	7.8780	7.8120
	28	5.6783	5.6365
	29	4.3565	4.3783
	30	3.8349	3.7510
	31	7.5665	7.4182

^{13}C-NMR: The calculated carbon chemical shifts are distributed within the range of 49–177 ppm. The carbon atom belonging to the carboxylic acid group (C_{20}) resonates around 177 ppm, corresponding to typical carbonyl carbons. The heteroaromatic carbons (C_4, C_8, C_{13}, and C_{15}) appear in the range of 150–175 ppm, reflecting their participation in conjugated C=N and C–S systems. Aromatic carbons (C_1, C_2, C_5, C_6, C_{10}–C_{12}) are observed between 125–138 ppm, corresponding to π-conjugated aromatic rings. The C17 atom, located within the thiazole ring, is shifted upfield (≈88 ppm) due to its proximity to the nitrogen atom and the resulting magnetic shielding effect. The aliphatic carbon (C_{18}) appears at around 49 ppm and corresponds to a methylene group bonded to a heteroatom. Examination of solvent effects revealed no significant chemical shift differences between DMSO and $CHCl_3$, indicating that the molecule possesses a rigid and stable structure.

^{1}H-NMR: Aromatic protons (H_{23}–H_{27}) are located within the δ 7.8–9.2 ppm range, exhibiting characteristic chemical shifts of π-conjugated aromatic systems (benzene and thiophene). The H_{29}–H_{30} protons appear between δ 3.7–4.4 ppm and correspond to aliphatic protons bonded to heteroatoms. The carboxylic acid proton (H_{31}) resonates downfield at approximately δ 7.4 ppm due to hydrogen-bonding effects. These results indicate that the molecule has a strong conjugated system, while solvent effects remain minimal.

3.4.2. CSS compound

Table 6. Calculated NMR Results of the CSS Compound

		DMSO	$CHCl_3$
	Atom	**Chemical Shift**	**Chemical Shift**
^{13}C-NMR	**1**	27.0896	27.0896
	2	29.6137	29.6137
	3	35.4952	35.4952
	4	88.2560	88.2560
	5	68.4023	68.4023
	6	39.7624	39.7624
	8	168.7631	168.7631
	10	155.4584	155.4584
	11	134.8517	134.8517
	12	136.5635	136.5635
	13	152.4035	152.4035
	15	171.8796	171.8796
	17	88.8182	88.8182
	18	49.0572	49.0572
	20	176.8292	176.8292
^{1}H-NMR	**23**	1.8630	1.8919
	24	1.7536	1.7289
	25	1.9128	1.8820
	26	2.0005	2.0438
	27	2.5752	2.6076
	28	2.2810	2.2329
	29	5.2148	5.1961
	30	4.7788	4.7129
	31	2.2763	2.2376
	32	1.7069	1.6967
	33	7.6984	7.6458
	34	7.8064	7.7486
	35	5.6079	5.5664
	36	4.2882	4.3099
	37	3.7803	3.6954
	38	7.5258	7.3691

^{13}C-NMR: The calculated carbon chemical shifts are distributed within the range of 27–177 ppm. The carbon atom belonging to the carboxylic acid group (C_{20}) resonates around 177 ppm, indicating a typical carbonyl carbon. The heteroaromatic carbons (C_8, C_{13}, and C_{15}) appear within the range of 152–172 ppm, reflecting the presence of conjugated C=N and C–S bonds. Additionally, the carbons located on the thiophene ring (C_{10}–C_{12}) resonate within 134–155 ppm, indicating aromatic character. The C_{17} atom, due to its proximity to the nitrogen atom in the ring, is shifted upfield and resonates around 88.8 ppm, suggesting a magnetic shielding effect. The aliphatic carbon C_{18} appears at approximately 49 ppm and corresponds to a methylene group bonded to a heteroatom. Carbons C_1–C_6 fall within the 27–88 ppm range and correspond to methyl and methylene groups within the aliphatic ring. No significant chemical shift differences were observed between DMSO and $CHCl_3$ solvents, indicating that the molecule possesses a stable structure.

^{1}H-NMR: Aromatic protons (H_{33}–H_{34}) are observed within the δ 7.6–7.8 ppm range, which is characteristic of π-conjugated aromatic systems. The carboxylic acid proton (H_{38}) appears in the δ 7.3–7.5 ppm region and shows a downfield shift due to hydrogen bonding effects. Aliphatic protons H_{23}–H_{28} generally appear in the δ 1.7–2.6 ppm range and correspond to methyl and methylene groups. Other methylene protons such as H_{36}–H_{37} resonate in the δ 3.7–4.3 ppm range, indicating the influence of nearby heteroatoms. No significant solvent-dependent chemical shift differences were observed between

DMSO and $CHCl_3$, suggesting that the structural integrity of the molecule is unaffected by solvent environment.

3.4.3. PSS compound

Table 7. Calculated NMR Results of the PSS Compound

		DMSO	$CHCl_3$
	Atom	**Chemical Shift**	**Chemical Shift**
^{13}C-NMR	**1**	162.4580	162.4580
	2	122.7985	122.7985
	3	129.2647	129.2647
	4	150.9918	150.9918
	5	149.9132	149.9132
	6	107.9619	107.9619
	8	166.4541	166.4541
	10	154.8808	154.8808
	11	131.6267	131.6267
	12	137.1867	137.1867
	13	150.2414	150.2414
	15	169.6481	169.6481
	17	88.7230	88.7230
	18	49.5830	49.5830
	21	63.0003	63.0003
	22	173.5918	173.5918
^{1}H-NMR	**25**	7.3325	7.3325
	26	8.1437	8.1437
	27	7.5211	7.5211
	28	7.7043	7.7043
	29	7.5923	7.5923
	30	5.4033	5.4033
	31	4.2831	4.2831
	32	3.6076	3.6076
	33	4.3361	4.3361
	34	3.9768	3.9768
	35	3.9786	3.9786
	36	6.9867	6.9867

^{13}C-NMR: The calculated carbon chemical shifts are distributed within the range of 49–174 ppm. The carbon atom belonging to the carboxylic acid group (C_{22}) resonates at around 173.6 ppm, corresponding to the characteristic region of carbonyl carbons. The heteroaromatic carbons (C_8, C_{13}, and C_{15}) appear in the range of 150–170 ppm, reflecting their participation in conjugated C=N and C–S systems. Aromatic carbons (C_1–C_6, C_{10}–C_{12}) are observed between 108–138 ppm, whereas aliphatic carbons (C_{18}, C_{21}) resonate in the higher field region (49–63 ppm), corresponding to methylene and methoxy environments. C_2, C_3, C_{11}, and C_{12} represent typical aromatic CH carbons. The C_{17} atom, located within the thiazole ring, is shifted upfield due to its proximity to the nitrogen atom and the resulting magnetic shielding effect.

^{1}H-NMR: Aromatic protons belonging to benzene and thiophene rings (H_{25}–H_{29}) are concentrated in the δ 7.3–8.1 ppm range, which is characteristic of π-conjugated systems. The H_{26} proton exhibits the most deshielded signal among them due to its close spatial position to the nitrogen atom. The methoxy group protons (H_{33}–H_{35}) are observed between δ 3.98–4.34 ppm. The carboxylic acid proton (H36) appears downfield at approximately δ 6.9 ppm, attributed to possible intermolecular hydrogen-bonding effects. These findings indicate that solvent-dependent chemical shift variations are minimal, suggesting that the molecule possesses a rigid and highly conjugated structure. Additionally, the downfield shift

observed in the carboxylic acid region further supports the presence of hydrogen-bonding interactions in solution.

3.5. Molecular Electrostatic Potential (MEP) Analysis

The molecular electrostatic potential (MEP) maps of all studied compounds were obtained using DFT calculations. MEP maps visually illustrate the distribution of electron density over the molecular surface and provide important insights into chemical reactivity, potential binding sites, and interaction tendencies.

In these maps, red regions indicate areas of high electron density (negative electrostatic potential), which correspond to nucleophilic centers susceptible to electrophilic attack. Conversely, blue regions represent areas of low electron density (positive electrostatic potential), which correspond to electrophilic sites prone to nucleophilic attack.

The analysis revealed that in all the molecules examined—TPSS, CSS, and PSS—the highest negative electrostatic potential is concentrated around the oxygen atoms of the carboxylic acid group (Figure 17). These regions exhibit strong nucleophilic character and are highly likely to interact with electrophilic species. Additionally, moderate negative potential was observed around the nitrogen atoms in the benzothiazole rings, indicating partial nucleophilic behaviour of these heterocyclic regions.

For the TPSS molecule, the effect of extended π-conjugation results in a homogeneous distribution of electrostatic potential over the molecular surface. This suggests that TPSS possesses a balanced and stable electronic structure, leading to more consistent behaviour in molecular interactions. In contrast, due to limited π-conjugation in the CSS molecule, the negative potential is more localized, resulting in selective regional reactivity. The pronounced blue and green areas on the ring regions indicate the presence of potential electrophilic attack sites.

In the PSS molecule, the electron-donating effect of the methoxy group leads to a slightly increased electron density around the aromatic ring. This demonstrates that the methoxy substituent modifies the electronic distribution of the molecule, differentiating its electronic properties from those of TPSS.

In conclusion, the balanced potential distribution of TPSS suggests enhanced molecular stability, while the localized negative regions in CSS indicate selective reactivity, and the methoxy group in PSS highlights an enriched electron density. These findings offer critical insights into how these molecules may behave in targeted applications.

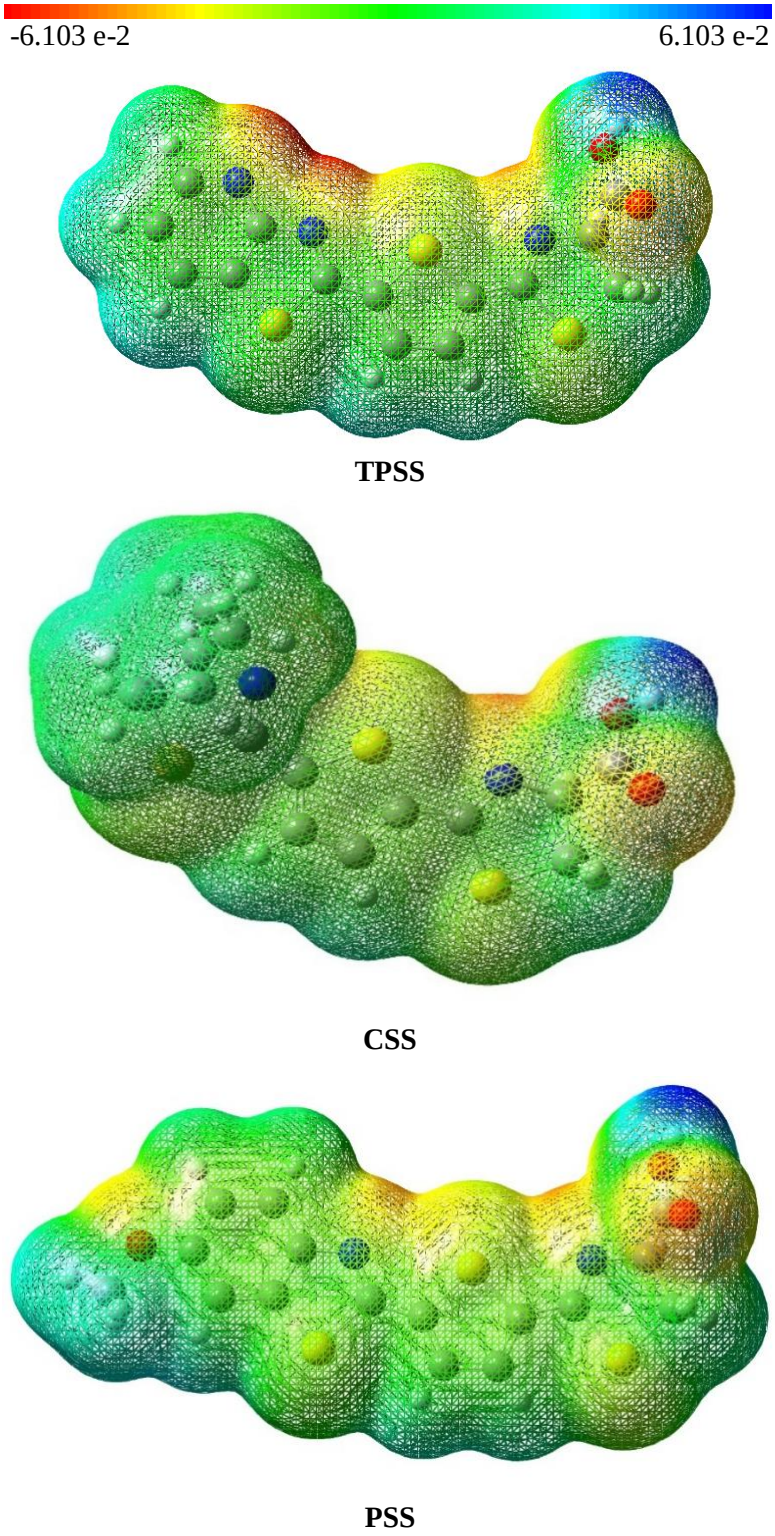

Figure 17. Molecular Electrostatic Potential (MEP) Maps of the Investigated Compounds

4. CONCLUSIONS

In this study, the structural and electronic properties of three different compounds containing thiazolopyridine (TPSS), cyclohexyl (CSS), and methoxybenzene (PSS) groups, derived from the natural luciferin structure, were thoroughly investigated using DFT and TD-DFT methods. Geometry optimizations revealed that the compounds generally exhibit planar structures, whereas the carboxylic acid group is oriented perpendicular to the main framework, partially disrupting conjugation. Dihedral angle and bond lengths analyses further supported this finding.

Examination of the HOMO–LUMO energy gaps showed that the PSS compound possesses a narrower energy gap, indicating a greater propensity for electronic transitions. TD-DFT calculated UV-Vis spectra demonstrated that PSS exhibits maximum absorption in the 340–430 nm range, consistent with π–π^* and n–π^* transitions. In the TPSS compound, the absorption maximum was slightly red-shifted due to differences in electron density distribution arising from its structural features. However, in the PSS molecule, the presence of a methoxy group with an electron-donating effect raises the HOMO energy level, making it the most red-shifted among the studied molecules. The observed blue shifts in CSS compound is attributed to their wider energy gaps.

IR spectral analyses indicated that characteristic peaks corresponding to carboxylic acid OH groups, C=N, aromatic/aliphatic C–H, and C=C vibrations were successfully predicted for all molecules. This confirms the accurate optimization of molecular structures and the agreement of theoretical expectations.

MEP maps revealed intense negative potential accumulation around the carboxylic acid group, indicating strong nucleophilic character in these regions. In PSS, the potential distribution was observed to be more homogeneous and balanced due to the extended conjugation.

In conclusion, the PSS compound stands out with its electronic transition efficiency, stable conformation, and homogeneous charge distribution. The obtained theoretical data provide valuable insights into the potential applicability of these molecules in fields such as organic electronics and biosensors. It is recommended that future experimental studies be conducted to validate the calculated values.

CONFLICT OF INTEREST

The authors stated that there are no conflicts of interest regarding the publication of this article.

CRediT AUTHOR STATEMENT

Sultan Funda Ekti: Supervision, Conceptualization, Methodology, Investigation, Writing – Review & Editing. **Sevgi Şen:** Formal analysis, Investigation, Writing – Original Draft.

REFERENCES

[1] Tang YQ, Liu YJ. Computational bioluminescence. Chin J Chem., 2021; 39 (1), 43–49. doi:10.1002/cjoc.202000436.

[2] Da Silva LP, Esteves Da Silva JCG. Computational studies of the luciferase light-emitting product: oxyluciferin. J Chem Theory Comput., 2011; 7. doi:10.1021/ct200003u.

[3] Fan F, Wood KV. Bioluminescent assays for high-throughput screening. Assay Drug Dev Technol., 2007; 5 (1), 127–136. doi:10.1089/adt.2006.053.

[4] Ugarova NN. Interaction of firefly luciferase with substrates and their analogs: a study using fluorescence spectroscopy methods. Photochem Photobiol Sci., 2008; 7 (2), 218–227. doi:10.1039/b712895a.

[5] Inouye S. Firefly luciferase: an adenylate-forming enzyme for multicatalytic functions. Cell Mol Life Sci., 2010; 67 (3), 387–404. doi:10.1007/s00018-009-0170-8.

[6] Li S, Ruan Z, Zhang H, Xu H. Recent achievements of bioluminescence imaging based on firefly luciferin-luciferase system. Eur J Med Chem., 2021; 211, 113111. doi:10.1016/j.ejmech.2020.113111.

[7] Wannlund J, DeLuca M, Stempel K, Boyer PD. Use of 14C-carboxyl-luciferin in determining the mechanism of the firefly luciferase catalyzed reactions. Biochem Biophys Res Commun., 1978; 81 (3), 987–992. doi:10.1016/0006-291X(78)91448-1.

[8] Shimomura O, Goto T, Johnson FH. Source of oxygen in the CO_2 produced in the bioluminescent oxidation of firefly luciferin. Proc Natl Acad Sci U S A., 1977; 74 (7), 2799–2802. doi:10.1073/pnas.74.7.2799.

[9] Hopkins TA, Seliger HH, White EH, Cass MW. Chemiluminescence of firefly luciferin. Model for the bioluminescent reaction and identification of the product excited state. J Am Chem Soc., 1967; 89 (26), 7148–7150. doi:10.1021/ja01002a076.

[10] Everything about luciferin-luciferase. GoldBio website. Accessed February 23, 2026. https://goldbio.com/articles/article/Everything-About-Luciferin-Luciferase.

[11] Liu YJ, Fang WH. Ab initio investigation on the structures and spectra of the firefly luciferin. Sci China B Chem., 2007; 50 (6), 725–730. doi:10.1007/s11426-007-0127-4.

[12] Chen SF, Liu YJ, Navizet I, Ferré N, Fang WH, Lindh R. Systematic theoretical investigation on the light emitter of firefly. J Chem Theory Comput., 2011; 7 (3), 798–803. doi:10.1021/ct200045q.

[13] Vreven T, Miller SC. Computational investigation into the fluorescence of luciferin analogues. J Comput Chem., 2019; 40 (2), 527–531. doi:10.1002/jcc.25745.

[14] Chattopadhyaya M, Alam MD. A theoretical study of one- and two-photon activity of D-luciferin. Computation, 2016; 4 (4), 43. doi:10.3390/computation4040043.

[15] Yu M, Liu YJ. Same luciferin in different luciferases emitting different-color light. A theoretical study on beetle bioluminescence. J Chem Theory Comput., 2020; 16 (6), 3904–3909. doi:10.1021/acs.jctc.0c00074.

[16] Reddy GR, Thompson WC, Miller SC. Robust light emission from cyclic alkylaminoluciferin substrates for firefly luciferase. J Am Chem Soc., 2010; 132 (39), 13586–13587. doi:10.1021/ja104525m.

[17] Mofford DM, Reddy GR, Miller SC. Aminoluciferins extend firefly luciferase bioluminescence into the near-infrared and can be preferred substrates over D-luciferin. J Am Chem Soc., 2014; 136 (38), 13277–13282. doi:10.1021/ja505795s.

[18] Satalkar V, et al. Computational investigation of substituent effects on the fluorescence wavelengths of oxyluciferin analogs. J Photochem Photobiol A Chem., 2022; 431, 114018. doi:10.1016/j.jphotochem.2022.114018.

[19] Yao Z, Zhang BS, Steinhardt RC, Mills JH, Prescher JA. Multicomponent bioluminescence imaging with a π-extended luciferin. J Am Chem Soc., 2020; 142 (33), 14080–14089. doi:10.1021/jacs.0c01064.

[20] Min CG, Leng Y, Yang XK, Huang SJ, Ren AM. Systematic color tuning of a family of firefly oxyluciferin analogues suitable for OLED applications. Dyes Pigments., 2016; 126, 202–208. doi:10.1016/j.dyepig.2015.12.004.

[21] Perepichka IF, Perepichka D. Thiophene-based materials for electroluminescent applications. Available at: https://www.researchgate.net/publication/266741294. Accessed February 23, 2026.

[22] Hehre WJ, Ditchfield R, Pople JA. Self-consistent molecular orbital methods. XII. Further extensions of Gaussian-type basis sets for use in molecular orbital studies of organic molecules. J Chem Phys., 1972; 56 (5), 2257–2261. doi:10.1063/1.1677527.

[23] Muz İ. Fluoroquinolone antibiotic adsorption on the functional C70 fullerenes: a computational insight on adsorbent applications. Bitlis Eren Univ Fen Bilim Derg., 2025; 14 (1), 385–397.

[24] Kurban M, Sertbakan ST, Muz İ. Computational analysis and experimental validation of a quinoline derivative for optoelectronic and pharmacological applications. Mater Today Commun., 2024; 39, 108642.

[25] Muz İ, Kurban M. Electronic transport and non-linear optical properties of hexathiopentacene (HTP) nanorings: a DFT study. J Electron Mater., 2020; 49 (5), 3282–3289.

[26] Frisch MJ, et al. Gaussian 09. Wallingford, CT: Gaussian, Inc.; 2009.

[27] Cossi M, Rega N, Scalmani G, Barone V. Energies, structures, and electronic properties of molecules in solution with the C-PCM solvation model. J Comput Chem., 2003; 24 (6), 669–681. doi:10.1002/jcc.10189.

[28] Merrick JP, Moran D, Radom L. An evaluation of harmonic vibrational frequency scale factors. J Phys Chem A., 2007; 111 (45), 11683–11700. doi:10.1021/jp073974n.

[29] Brédas JL, Norton JE, Cornil J, Coropceanu V. Molecular understanding of organic solar cells: the challenges. Acc Chem Res., 2009; 42 (11), 1691–1699. doi:10.1021/ar900099h.

[30] Suenaga M. Facio: new computational chemistry environment for PC GAMESS. J Comput Chem Jpn., 2005; 4 (1), 25–32. doi:10.2477/jccj.4.25.